

## Morphodynamics of barchan and dome dunes under variable wind regimes

Xin Gao<sup>1</sup>, Cyril Gadal<sup>2</sup>, Olivier Rozier<sup>2</sup>, Clément Narteau<sup>2</sup>

- <sup>1</sup>) State Key Laboratory of Desert and Oasis Ecology, Xinjiang Institute of Ecology and Geography, Chinese Academy of Sciences, 818 South Beijing Road, Urumqi 830011, Xinjiang, China.
- <sup>2</sup>) Equipe de Dynamique des Fluides Géologiques, Institut de Physique du Globe de Paris, Sorbonne Paris Cité, Univ Paris Diderot, UMR 7154 CNRS, 1 rue Jussieu, 75238 Paris Cedex 05, France.

### Contents

<b>1</b>	<b>Wind data, transport properties and dune orientations in terrestrial dune systems</b>	<b>2</b>
1.1	Wind data . . . . .	2
1.2	Saturated flux on a flat sand bed . . . . .	2
1.3	Sand flux at the crest of dunes . . . . .	4
1.4	Dune orientation $\alpha_I$ in the bed instability mode . . . . .	5
1.5	Dune orientation $\alpha_F$ in the fingering mode . . . . .	5
<b>2</b>	<b>Estimation of dune asymmetry</b>	<b>5</b>
<b>3</b>	<b>The model of dune contour</b>	<b>6</b>
<b>4</b>	<b>Formation of steady-state dune patterns in the numerical dune model</b>	<b>7</b>
<b>5</b>	<b>Growth rate with respect to dune orientation under unimodal wind regimes</b>	<b>7</b>
<b>6</b>	<b>Steady-state dome dune morphodynamics in Mauritania</b>	<b>8</b>

**Table DR1:** Sand transport properties and the predicted crest orientations for the terrestrial dune systems shown in Fig. DR1. These results are produced using the wind data of the ERA-Interim project for the period from the 1/1/1979 to the 31/12/2016. The numerical procedure to estimate all these parameters is described in details in Sec. 1. All fluxes and dune orientations are measured in degree anticlockwise from East.  $S_d$  is the dispersion of sand flux orientation measured in angular units.

Site	Latitude	Longitude	$DP$ m <sup>2</sup> /yr	$RDP$ m <sup>2</sup> /yr	$RDP/DP$	$RDD$ [360°]	$S_d$ °	$\alpha_I$ [180°]	$\alpha_F$ [360°]	$C_v$
(a)	16°41′N	17°54′E	55.3	49.1	0.89	216.3	34.2	127.6	215.6	0.3598
(b)	21°14′N	27°12′E	18.1	16.6	0.92	245.3	25.6	155.4	245.6	0.3426
(c)	26°46′N	30°00′E	22.3	17.9	0.80	281.9	44.3	5.8	284.8	0.1710
(d)	26°41′N	16°26′W	95.7	82.7	0.86	257.8	32.4	168.9	256.9	0.2634
(e)	20°28′N	16°17′W	109.2	89.2	0.82	272.0	41.5	4.2	271.1	0.1874
(f)	21°07′N	14°07′W	51.5	41.6	0.81	242.8	42.9	152.7	241.0	0.2391
(g)	19°30′N	15°28′W	52.7	34.3	0.65	258.6	62.5	160.3	258.0	0.2009
(h)	22°11′N	12°05′W	15.6	12.5	0.80	216.0	77.8	121.5	217.5	0.1321
(i)	19°53′N	14°09′W	38.6	28.8	0.74	240.0	45.7	153.8	237.7	0.2093
(j)	18°59′N	14°09′W	43.3	27.6	0.64	239.3	69.9	134.9	239.6	0.1858
(k)	24°30′N	27°07′E	40.0	20.4	0.51	246.2	86.0	126.3	248.2	0.1730
(l)	40°14′N	83°31′E	12.7	8.7	0.69	278.8	66.2	5.8	280.1	0.1523

## 1 Wind data, transport properties and dune orientations in terrestrial dune systems

Fig. DR1 shows the 12 dune fields studied in the main manuscript. Transport properties and the predicted dune orientations of all these terrestrial dune systems are presented in Tab. DR1. In what follows, we describe the wind data and the method used to derive these quantities.

### 1.1 Wind data

The wind data used in the main manuscript are extracted from the ERA-Interim reanalysis, the latest global atmospheric data assimilation model produced by the European Centre for Medium-Range Weather Forecasts (ECMWF) (Dee et al., 2011). The ERA-Interim data are produced for all locations on Earth. This model extends back to 1979 and has been continued to present with a horizontal spatial resolution of  $0.25^\circ \times 0.25^\circ$  and a time resolution of 6 hours (0: 00, 6: 00, 12: 00, 18: 00 UTC). For this period of time and these resolutions, we use here the azimuthal and meridional components of the 10 m wind data.

### 1.2 Saturated flux on a flat sand bed

Wind measurements provide the wind speed  $u_i$  and direction  $\vec{x}_i$  at different times  $t_i$ ,  $i \in [1; N]$ . For each time step  $i$ , we calculate the shear velocity

$$u_*^i = \frac{u_i \kappa}{\log(z/z_0)}, \quad (1)$$

where  $z = 10$  m is the height at which the wind data has been computed,  $z_0 = 10^{-3}$  m the characteristic surface roughness and  $\kappa = 0.4$  the von-Kármán constant. The threshold shear velocity value for motion inception can be determined using the formula calibrated by Iversen and Rasmussen (1999)

$$u_c = 0.1 \sqrt{\frac{\rho_s}{\rho_f} g d}. \quad (2)$$

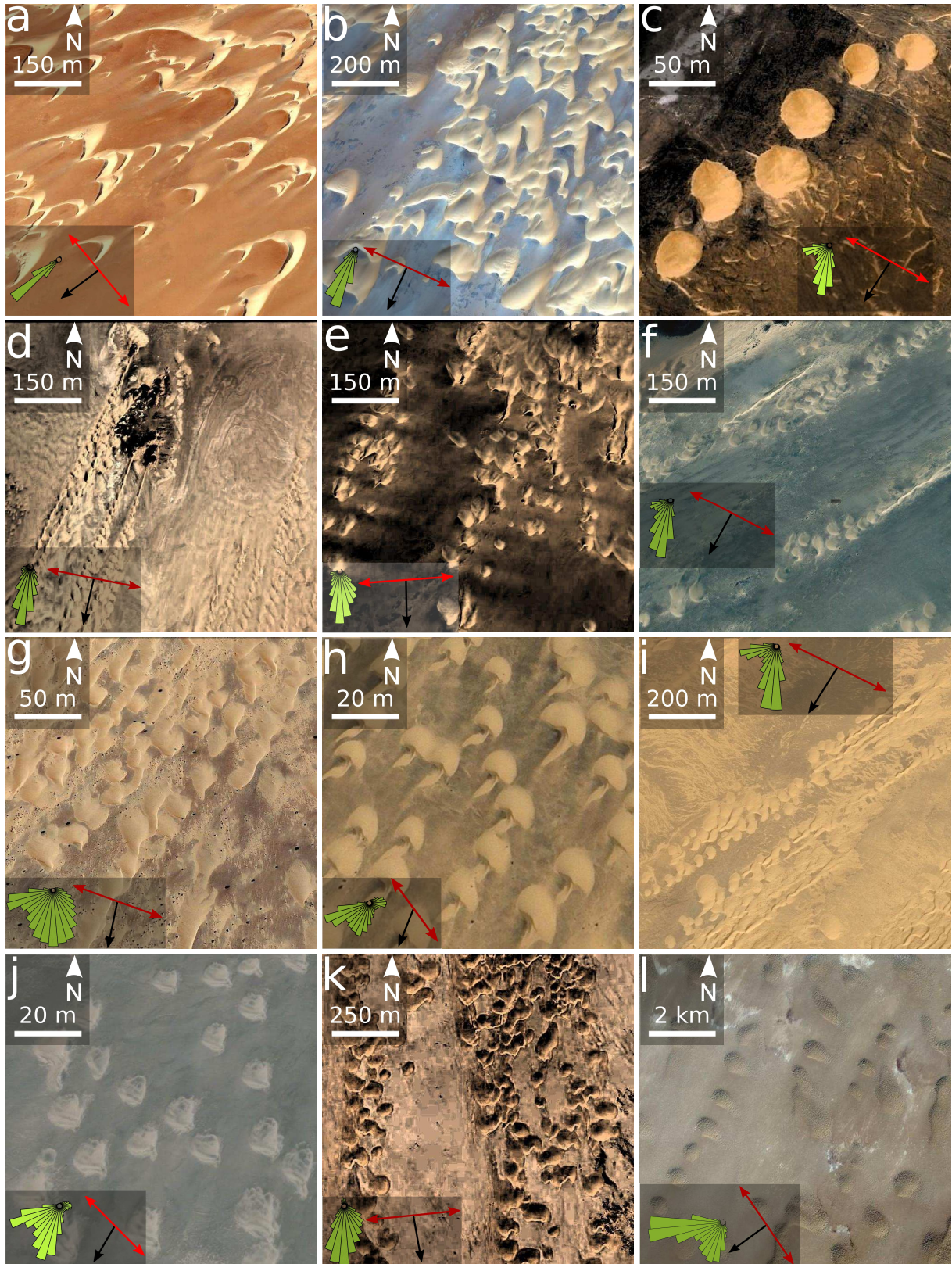


**Figure DR1: Barchan and dome dunes in terrestrial dune systems.** (a) Barchan dunes in Chad ( $16^{\circ}41'N$ ,  $17^{\circ}54'E$ ). (b) Barchan dunes in Sudan ( $21^{\circ}14'N$ ,  $27^{\circ}12'E$ ). (c) Dome dunes in Egypt ( $26^{\circ}46'N$ ,  $30^{\circ}00'E$ ). (d-j) Dome dunes in Mauritania:  $26^{\circ}41'N$ ,  $16^{\circ}26'W$  (d);  $20^{\circ}28'N$ ,  $16^{\circ}17'W$  (e);  $21^{\circ}07'N$ ,  $14^{\circ}07'W$  (f);  $19^{\circ}30'N$ ,  $15^{\circ}28'W$  (g);  $22^{\circ}11'N$ ,  $12^{\circ}05'W$  (h);  $19^{\circ}53'N$ ,  $14^{\circ}09'W$  (i);  $18^{\circ}59'N$ ,  $14^{\circ}09'W$  (j). (k) Dome dunes in Egypt ( $24^{\circ}30'N$ ,  $27^{\circ}07'E$ ). (l) Giant dome dunes in northern Taklamakan (China,  $40^{\circ}14'N$ ,  $83^{\circ}31'E$ ). For each dune field, the inset shows the sand flux rose and the predicted dune orientations for the two dune growth mechanisms introduced by Courrech du Pont et al. (2014) and Gao et al. (2015).

Using the gravitational acceleration  $g = 9.81 \text{ m s}^{-2}$ , the grain to fluid density ratio  $\rho_s/\rho_f = 1.97 \times 10^3$  and the grain diameter  $d = 180 \text{ } \mu\text{m}$ , we find  $u_c = 0.19 \text{ m s}^{-1}$ , which corresponds to a threshold wind speed of  $4.37 \text{ m s}^{-1}$  ten meters above the ground. For each time step  $i$ , the saturated sand flux vectors  $\vec{Q}_i$  on a flat sand bed can be calculated from the relationship proposed by Ungar and Haff (1987)

$$Q_{\text{sat}}(u_*) = \begin{cases} 25 \frac{\rho_f}{\rho_s} \sqrt{\frac{d}{g}} (u_*^2 - u_c^2) & \text{for } u_* \geq u_c, \\ 0 & \text{else.} \end{cases} \quad (3)$$

From the individual saturated sand flux vectors  $\vec{Q}_i$ , it is possible to estimate the mean sand flux on a flat erodible bed, also called the drift potential

$$DP = \frac{\sum_{i=2}^N \|\vec{Q}_i\| \delta t_i}{\sum_{i=2}^N \delta t_i}. \quad (4)$$

where

$$\delta t_i = t_i - t_{i-1}.$$

Averaged over the entire time period, this quantity does not take into account the orientation of the sand fluxes (Fryberger and Dean, 1979). Then, it is also important to calculate the resultant drift potential,

$$RDP = \frac{\left\| \sum_{i=2}^N \vec{Q}_i \delta t_i \right\|}{\sum_{i=2}^N \delta t_i}, \quad (5)$$

which is the norm of the sum of all individual flux vectors. This quantity is strongly dependent on the function of wind directionality.

Using Eqs. 4 and 5,  $DP$  and  $RDP$  have units of sand flux. The  $RDP/DP$ -value is a non-dimensional parameter which is often used to characterize the directional variability of the wind regimes (Pearce and Walker, 2005; Tsoar, 2005):  $RDP/DP \rightarrow 1$  indicates that sediment transport tends to be unidirectional;  $RDP/DP \rightarrow 0$  indicates that most of the transport components cancel each other. Finally,  $RDD$  is the resultant drift direction, i.e., the direction of  $\sum \vec{Q}_i \delta t_i$ .

The standard deviation of the sand flux distribution writes

$$S_d = \sqrt{\frac{\sum_{i=2}^N \|\vec{Q}_i\| \eta_i^2 (t_i - t_{i-1})}{\sum_{i=2}^N \|\vec{Q}_i\| (t_i - t_{i-1})}}, \quad (6)$$

where  $\eta_i = \theta_i - \alpha_F$  is the angle between wind orientation and the  $RDD$ . As the dimensionless  $RDP/DP$ -value, we can use the  $S_d$ -value measured in angular units to characterize the variability in wind directionality.

### 1.3 Sand flux at the crest of dunes

The presence of topography accelerates the wind so that the sand flux over a dune depends on the dune shape. For 2D turbulent flows over low hills, Jackson and Hunt (1975) show analytically that the wind velocity increase at the top of the hill, the so-called speed-up factor,

is approximately proportional to the hump aspect ratio. Hence, considering the angle  $\theta_i$  of the flux vector  $\vec{Q}_i$  on a flat sand bed and the crest orientation  $\alpha$ , the sand flux vectors  $\vec{Q}_i^c$  at the crest of dunes become

$$\vec{Q}_i^c = \vec{Q}_i (1 + \gamma |\sin(\theta_i - \alpha)|) \quad (7)$$

where

$$\gamma = \beta \frac{H}{W}, \quad (8)$$

is the flux-up ratio,  $W$  the width of the dune,  $H$  the height of the dune and  $\beta$  a dimensionless coefficient that accounts for all the other physical ingredients (e.g., roughness) that affect the speed-up.

#### 1.4 Dune orientation $\alpha_I$ in the bed instability mode

Where there is no limit in sand availability, in transport-limited situations, dunes grow in height selecting the orientation for which the gross bedform-normal transport is maximum. This is described as the bed instability mode by Courrech du Pont et al. (2014).

To estimate the dune orientation  $\alpha_I$  in the bed instability mode, we do not take into account from which side of the dune the wind blows. In fact, all winds contribute to dune growth as soon as they have a normal to crest component of transport. Thus, linear bedforms can develop perpendicularly to the maximum gross bedform-normal transport (Rubin and Hunter, 1987) and extend laterally from both ends as long as there is no limit in sediment availability.

Considering the angle  $\theta_i$  of the flux vector  $\vec{Q}_i^c$ , we calculate  $Q_{\perp}(\alpha)$ , the total sand flux perpendicular to the crest for all possible crest orientations  $\alpha \in [0; \pi]$ . Then, we identify the maximum value of  $Q_{\perp}(\alpha)$  that corresponds to the most probable crest orientation  $\alpha_I$  of dunes in the bed instability mode. Note that this procedure is the same as the gross bedform-normal transport rule proposed by Rubin and Hunter (1987), except that we take into account the sand flux at the crest of dunes (i.e.,  $\gamma \neq 0$ ). As detailed in Courrech du Pont et al. (2014) and Gao et al. (2015), it may significantly change dune orientations.

#### 1.5 Dune orientation $\alpha_F$ in the fingering mode

In zones partially starved of mobilizable sediment, a dune can also elongate in the direction of the resultant sand flux at the crest. This is described as the fingering mode. Where dunes grow from fixed sources of sediment, finger dunes select the orientation for which the normal-to-crest components of transport cancel each other (Courrech du Pont et al., 2014; Lucas et al., 2015; Gao et al., 2015).

To estimate the dune orientation  $\alpha_F$  in the fingering mode, we calculate  $Q_{\perp}(\alpha)$  and  $Q_{\parallel}(\alpha)$ , the total sand flux perpendicular and parallel to the crest for all possible crest orientations  $\alpha \in [0; 2\pi]$ . In practice,  $\alpha_F$  is the orientation for which the sediment flux perpendicular to the crest vanishes (i.e.,  $Q_{\perp}(\alpha) = 0$ ) and for which the flux parallel to the dune is positive (i.e.,  $Q_{\parallel}(\alpha) > 0$ ). If more than one solution exists, we look for the angle at which the  $Q_{\parallel}$ -value is maximum. By definition, when there is no feedback of topography on the flow (i.e.,  $\gamma = 0$ ), the orientation of the fingering mode  $\alpha_F$  is given by the resultant sand transport direction (also called the *RDD*). There is therefore a range of possible dune orientations from  $\gamma = 0$  to  $\gamma \rightarrow +\infty$ . In a vast majority of cases, a  $\gamma$ -value close to 1.6 gives reasonable estimates of dune orientation (Gao et al., 2015).

## 2 Estimation of dune asymmetry

Here we introduce the method for the calculation of  $c_v$ , a parameter accounting for dune asymmetry. First, the topography  $h$  allows us to get the contour line of the dune (Fig. DR2)

by selecting the height at a certain threshold. This line form an ensemble of points  $(x_i, y_i)$  such that :

$$h(x_i, y_i) = h_{\text{th}}. \quad (9)$$

In the numerical model, the threshold is taken at  $h_{\text{th}} = h_{\text{flat}} + 2 l_0$ , where  $h_{\text{flat}}$  is the height of the flat non-erodible ground and  $l_0$  the elementary length scale of the cellular space. On satellite images the color contrast determines the contour of the dunes. Considering points regularly distributed on the contour, the center of mass  $(x, y)$  is obtained by averaging:

$$x = \langle x_i \rangle \quad y = \langle y_i \rangle. \quad (10)$$

The dune asymmetry  $c_v$  is defined as

$$c_v = \frac{\sigma}{\langle r_i \rangle}, \quad (11)$$

where  $r_i = \sqrt{(x_i - x)^2 + (y_i - y)^2}$  is the distance of each point of the contour to the center of mass, and  $\sigma$  the standard deviation of these distances. Fig. DR2 shows two examples, from the numerical model and in terrestrial dune fields. In the numerical model, the topography file is obtained by averaging over time the topography of the steady state dome. For the field data, satellite images are converted into pseudo color. Using a threshold color value, which may differ from an image to another, the  $c_v$ -value is obtained by averaging over at least 20 dunes.

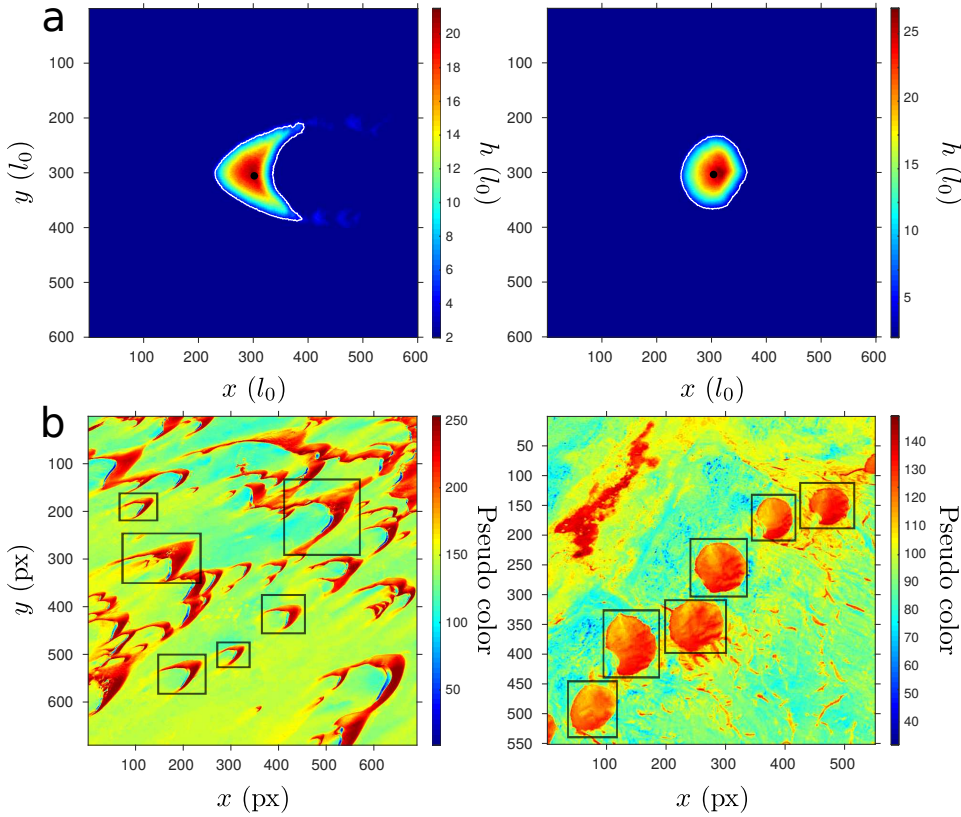


**Figure DR2: Estimation of  $c_v$ -value in (a) the numerical model and (b) terrestrial dune fields.** White lines in (a) are contour lines at height of  $2 l_0$  above the flat non-erodible bed. Black dots show the location of the centers of mass. In terrestrial dune fields, the  $c_v$ -value is obtained by averaging over at least 20 contours extracted from specific portions of the image (black rectangles in (b)).

### 3 The model of dune contour

In addition to the dune asymmetry parameter  $c_v$ , a geometric model of dune contour is introduced to capture the transition between crescentic and rounded shapes. In this model, the upstream part of the contour is a semicircle of diameter  $AB = 2r$  and center  $O$ . The downstream

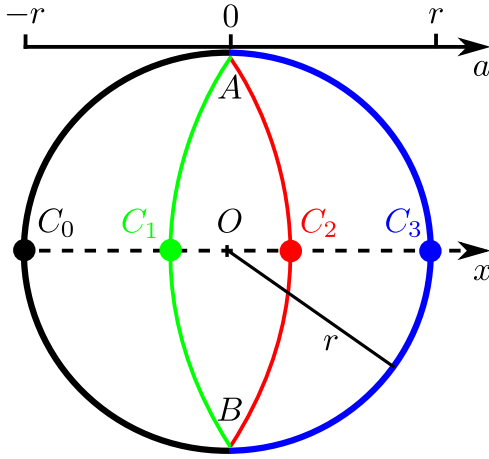


**Figure DR3: A geometric model for planar dune contour.** The  $x$ -axis is in the direction of the resultant transport. The upstream part is a semicircle of diameter  $AB = 2r$ , and the downstream part is an arc passing through  $A$  and  $B$  of sagitta  $a = OC_i$  with  $i \in \{0, 1, 2, 3\}$ . The different colors correspond to different dune shapes. For  $-r < a < 0$  (black and green arcs), the dune takes a crescentic shape. For  $0 < a < r$  (red and blue arcs), the dune takes an ovoid shape.

part is an arc passing through the points  $A$  and  $B$ . The intersection of this arc with the  $x$ -axis, of origin  $O$  and directed perpendicularly to the chord  $AB$ , is noted  $C$  (Fig. DR3).  $OC$  is the sagitta and the variable  $a = x_C$  can be used to characterize the dune contour. From the semicircle of diameter  $r$  and center  $O$  ( $a = -r$ ) to the half-disk ( $a = 0$ ), the dune contour has a crescentic shape. From the half-disk to the the plain disk ( $a = r$ ), it takes an ovoid shape.

In this geometric model, the dune asymmetry  $c_v$  presented in the previous section (Sec. 2) can also be calculated as a function of  $a$ . The transition between barchan and dome shapes can be inferred from this relation by taking the value of  $c_v$  in  $a = 0$ . Stacking the data points  $c_v = f(S_d)$  with the theoretical curve  $c_v = g(a)$  on the same figure also allows to get a relationship between the  $S_d$  and  $a$ .

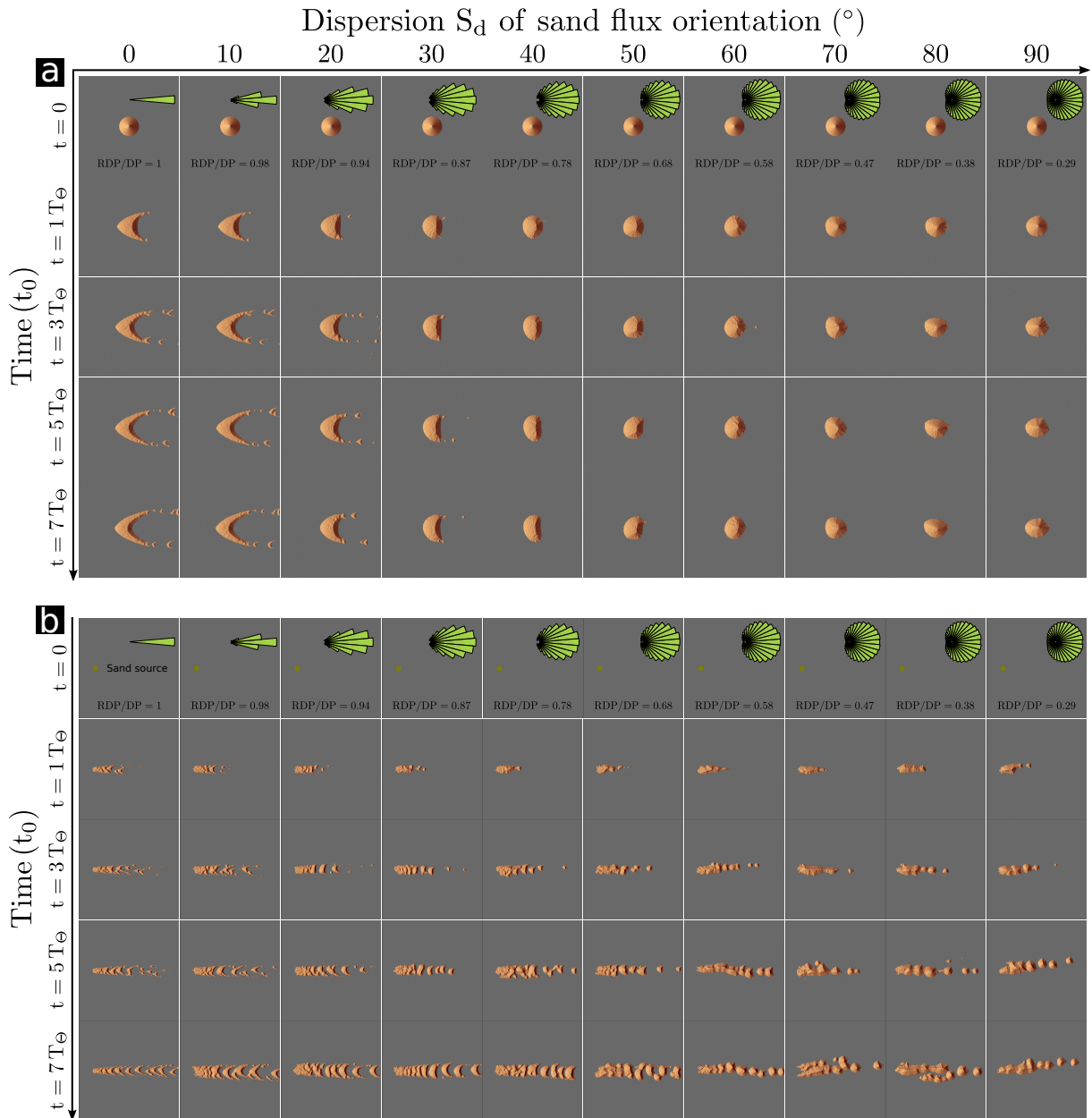
## 4 Formation of steady-state dune patterns in the numerical dune model

Fig. DR4 shows the formation of steady-state dune patterns in the numerical dune model starting from a conical sand pile (Fig. DR4a) or a localized circular sand source (Fig. DR4b). For an increasing standard deviation  $S_d$  of a normal distribution of sand flux orientation, there is a transition from barchan to dome dunes for  $S_d \geq 40^\circ$ . Below this value, the steady-state bedforms exhibit a permanent slipface perpendicular to the resultant transport. This alignment corresponds to the dune orientation in the bed instability mode. Theoretically, there is an abrupt transition of dune alignment  $\alpha_I$  of the bed instability mode at  $S_d = 83.3^\circ$ . The  $\alpha_I$  switches of  $90^\circ$  (from  $90^\circ$  to  $0^\circ$ ) to take the orientation of the fingering mode, which is always parallel to the resultant transport direction. These two modes of dune orientation explain the emergence of transient slipfaces and linear dune features in dome dune fields.

## 5 Growth rate with respect to dune orientation under unimodal wind regimes

Following Courrech du Pont et al. (2014) and Gao et al. (2015), the growth rate  $\sigma$  is considered to be proportional to the sum of the normal to crest component of transport. Obviously, it varies according to the orientation  $\alpha$  of the dune. According to the notation used in Sec. 1, this dune growth rate writes

$$\sigma(\alpha) \propto \frac{\sum_{i=2}^N \left\| \vec{Q}_i \right\| \left( |\sin(\alpha - \theta_i)| + \gamma \sin^2(\alpha - \theta_i) \right) (t_i - t_{i-1})}{HW \sum_{i=2}^N (t_i - t_{i-1})}, \quad (12)$$



**Figure DR4: Formation of steady-state dune patterns in the numerical dune model.** Different columns are associated with different standard deviation  $S_d$  of a normal distribution of sand flux orientation (see flux roses). The initial condition is either (a) a conical sand pile with a radius of  $60 l_0$  and a height of  $40 l_0$ , or (b) a circular source of sediment with a diameter of  $15 l_0$ .  $l_0$  is the elementary length scale of the cellular space. All simulations have horizontal length of  $600 l_0$  and height of  $100 l_0$ .  $T_\theta = 410^3 t_0$  is the period of wind reorientation.

where  $H$  is the dune height and  $W$  its width.

Fig. DR5 shows the normalized dune growth rate with respect to both dune orientation and the standard deviation  $S_d$  of a normal distribution of sand flux orientation. Numerical simulations show that barchan dunes occur for  $S_d < 30^\circ$ , a range of values for which there is a clear maximum growth rate. For  $S_d > 50^\circ$ , the dependence of the growth rate on dune orientation is weak and, as predicted by the steady-state dome dune morphology of the numerical simulations, there is no selection in dune orientation.

## 6 Steady-state dome dune morphodynamics in Mauritania

Using the two satellite images shown in Fig. 4A of the main manuscript, we measure the migration rate and width of 210 steady-state dome dunes in Mauritania ( $18^\circ 59' N$ ,  $14^\circ 09' W$ ).

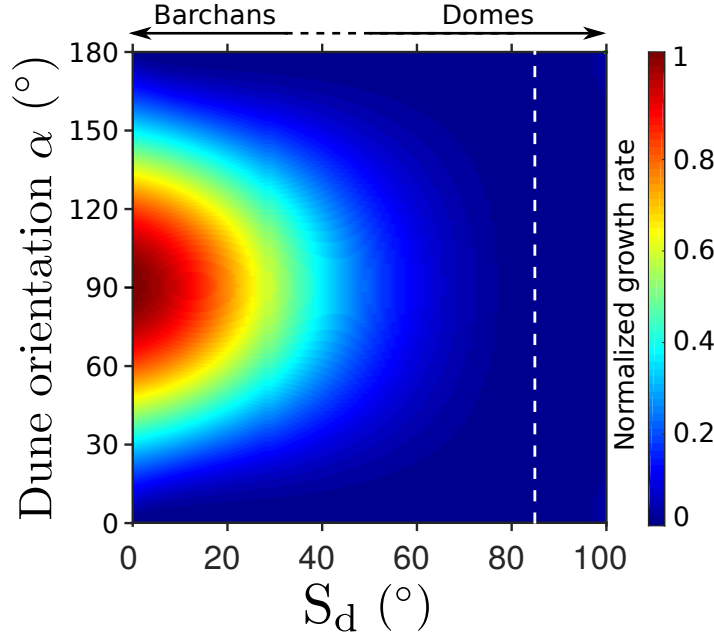


**Figure DR5: Selection of dune orientation under unimodal wind regimes.** Normalized growth rate with respect to both dune orientation and the standard deviation  $S_d$  of a normal distribution of sand flux orientation. The dashed white line corresponds to the  $S_d$ -value for which the growth rate is constant for all orientations ( $S_d = 83.3^\circ$ ). This is also the value for which the predicted orientation of the bed instability mode switches of  $90^\circ$ , from a transverse to a longitudinal alignment.

The width distribution shows an unique peak at 40 m and a small dispersion that suggest a selection in size within the dome dune field (Fig. DR6a). The classical relations between migration rate and dune height shown in Figs. DR6a and DR6b give a sediment flux at the crest of  $42.9 \text{ m}^2/\text{yr}$  considering a constant windward slope of  $10^\circ$  (i.e.,  $H = W \tan(10^\circ)/2$ ).

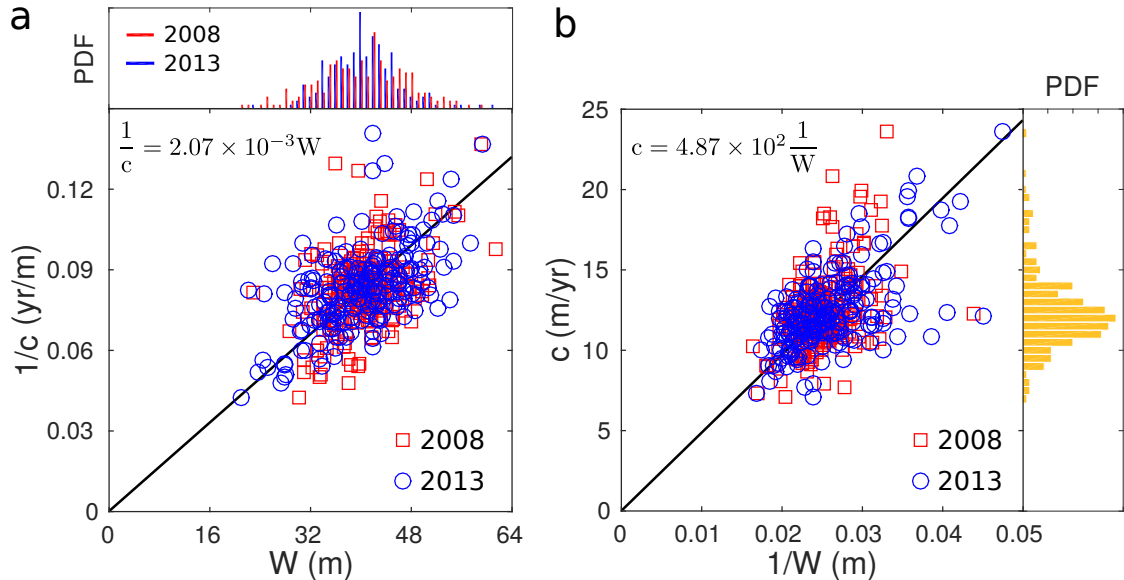


**Figure DR6: Relationships between migration rate and dune width in Mauritania.** Dune migration rate and width are estimated from the dome dune field in Mauritania shown in Fig. 4A of the main manuscript at two different times ( $18^\circ 59' \text{N}$ ,  $14^\circ 09' \text{W}$ ). (a) Inverse of the migration speed with respect to dune width. The measurements of dune width for the two different times are shown as marginal distributions on the top. These distributions shows a well-defined mode indicating that there is a selection of dune size. (b) Migration speed with respect to the inverse of dune width. The measurements of dune migration rate are shown as a marginal distribution on the right. In practice, we measure a distance of migration between the two times.

## References

- Courech du Pont, S., Narteau, C., and Gao, X., 2014, Two modes for dune orientation: *Geology*, v. 42, no. 9, p. 743–746.
- Dee, D., Uppala, S., Simmons, A., Berrisford, P., Poli, P., Kobayashi, S., Andrae, U., Balmaseda, M., Balsamo, G., Bauer, P., et al., 2011, The ERA-interim reanalysis: Configuration and performance of the data assimilation system: *Q. J. Roy. Meteorol. Soc.*, v. 137, no. 656, p. 553–597.
- Fryberger, S.G., and Dean, G., 1979, Dune forms and wind regime: A study of global sand seas, US Geological Survey, v. 1052, p. 137–169.
- Gao, X., Narteau, C., Rozier, O., and Courech du Pont, S., 2015, Phase diagrams of dune shape and orientation depending on sand availability: *Sci. Rep.*, v. 5, p. 14,677, doi: 10.1038/srep14677.
- Iversen, J.D., and Rasmussen, K.R., 1999, The effect of wind speed and bed slope on sand transport: *Sedimentology*, v. 46, no. 4, p. 723–731.
- Jackson, P., and Hunt, J., 1975, Turbulent wind flow over a low hill: *Q. J. Roy. Meteorol. Soc.*, v. 101, no. 430, p. 929–955.
- Lucas, A., Narteau, C., Rodriguez, S., Rozier, O., Callot, Y., Garcia, A., and Courech du Pont, S., 2015, Sediment flux from the morphodynamics of elongating linear dunes: *Geology*, v. 43, no. 11, p. 1027–1030.
- Pearce, K.I., and Walker, I.J., 2005, Frequency and magnitude biases in the ‘Fryberger’ model, with implications for characterizing geomorphically effective winds: *Geomorphology*, v. 68, no. 1, p. 39–55.
- Rubin, D., and Hunter, R., 1987, Bedform alignment in directionally varying flows: *Science*, v. 237, no. 4812, p. 276–278.
- Tsoar, H., 2005, Sand dunes mobility and stability in relation to climate: *Physica A*, v. 357, no. 1, p. 50–56.
- Ungar, J., and Haff, P., 1987, Steady state saltation in air: *Sedimentology*, v. 34, no. 2, p. 289–299.